Spectral and Broadband Longwave Downwelling Radiative Fluxes, Cloud Radiative Forcing, and Fractional Cloud Cover over the South Pole

MICHAEL S. TOWN

Department of Atmospheric Sciences, University of Washington, Seattle, Washington

VON P. WALDEN

Department of Geography, University of Idaho, Moscow, Idaho

STEPHEN G. WARREN

Department of Atmospheric Sciences, University of Washington, Seattle, Washington

(Manuscript received 12 July 2004, in final form 30 March 2005)

ABSTRACT

Annual cycles of downwelling broadband infrared radiative flux and spectral downwelling infrared flux were determined using data collected at the South Pole during 2001. Clear-sky conditions are identified by comparing radiance ratios of observed and simulated spectra. Clear-sky fluxes are in the range of 110–125 W m^{-2} during summer (December–January) and 60–80 W m^{-2} during winter (April–September). The variability is due to day-to-day variations in temperature, strength of the surface-based temperature inversion, atmospheric humidity, and the presence of "diamond dust" (near-surface ice crystals). The persistent presence of diamond dust under clear skies during the winter is evident in monthly averages of clear-sky radiance.

About two-thirds of the clear-sky flux is due to water vapor, and one-third is due to CO_2, both in summer and winter. The seasonal constancy of this approximately 2:1 ratio is investigated through radiative transfer modeling. Precipitable water vapor (PWV) amounts were calculated to investigate the H_2O/CO_2 flux ratio. Monthly mean PWV during 2001 varied from 1.6 mm during summer to 0.4 mm during winter. Earlier published estimates of PWV at the South Pole are similar for winter, but are 50% lower for summer. Possible reasons for low earlier estimates of summertime PWV are that they are based either on inaccurate hygristor technology or on an invalid assumption that the humidity was limited by saturation with respect to ice.

The average fractional cloud cover derived from the spectral infrared data is consistent with visual observations in summer. However, the wintertime average is 0.3–0.5 greater than that obtained from visual observations. The annual mean of longwave downwelling cloud radiative forcing (LDCRF) for 2001 is about 23 W m^{-2} with no apparent seasonal cycle. This is about half that of the global mean LDCRF; the low value is attributed to the small optical depths and low temperatures of Antarctic clouds.

1. Introduction

The polar regions are of significant importance to earth's climate. They emit more energy to space in the form of infrared radiation than they absorb from sunlight, and thus act as heat sinks for the climate system. This cooling helps drive the general circulation of the earth's atmosphere.

Despite Antarctica's importance to climate, it is still a relatively poorly characterized continent, particularly in the interior. Field studies performed in the late 1950s and 1960s still represent the current knowledge of the climate of the Antarctic interior (Dalrymple 1966; Kuhn et al. 1975, 1977; Schwerdtfeger 1984). Although major efforts have been undertaken to rectify the Antarctic data void by populating remote parts of Antarctica with automatic weather stations and routine observations at permanent science research stations, some

Corresponding author address: Michael S. Town, Dept. of Atmospheric Sciences, Box 351640, University of Washington, Seattle, WA 98195-1640.
E-mail: mstown@atmos.washington.edu

TABLE 1. Acronyms of parameters discussed in text.

Acronym	Definition	Units
CSR	Clear-sky radiance ratio	Fraction
FCC	Fractional cloud cover	%
$FCC_{APP\text{-}x}$	FCC derived from APP-x observations	%
FCC_{ISCCP}	FCC derived from ISCCP observations	%
FCC_{PAERI}	FCC derived from PAERI observations	%
FCC_{pyr}	FCC derived from pyrgeometer observations	%
FCC_{vis}	FCC from visual observations	%
FOV	Field-of-view	Radians
LDF	Longwave downwelling flux	W m^{-2}
LDF_{clear}	Longwave downwelling, clear-sky flux	W m^{-2}
LDF_{all}	Longwave downwelling, all-sky flux	W m^{-2}
LDCRF	Longwave downwelling cloud radiative forcing	W m^{-2}
LNCRF	Longwave net cloud radiative forcing	W m^{-2}
LNF	Longwave net flux	W m^{-2}
LUF	Longwave upward flux	W m^{-2}
MR	Mixing ratio	Unitless
RH_w	Relative humidity with respect to water	%
RR	Radiance ratio	Fraction
RU	Radiance unit	mW m^{-2} sr^{-1} $(cm^{-1})^{-1}$
T	Temperature	°C or K

key parameters of the Antarctic climate are still not well known.

Basic variables of atmospheric composition such as atmospheric humidity and fractional cloud cover (FCC), as well as the consequent downwelling infrared radiation spectra, are still poorly known quantities over the East Antarctic Plateau. Until recently, atmospheric humidity measurements made at low temperatures were not reliable (Elliott and Gaffen 1991; Miloshevich et al. 2001). There is some hope that Vaisala's Humicap radiosonde sensors are performing better under Antarctic conditions than the previous hygristor technology historically used on radiosondes (Hudson et al. 2004). FCC is difficult to estimate at high latitudes, particularly during the polar night (Hahn et al. 1995; Curry et al. 1996). Thus aspects of the climate related to clouds, such as the effect of clouds on the surface radiation budget, are also poorly characterized for the Antarctic interior.

FCC has been identified as an important and poorly predicted parameter in forecasts of Antarctic climate (Hines et al. 1999, 2004). It is important for closing the surface heat budget (Pavolonis and Key 2003), but recent efforts have been relatively unsuccessful at estimating the magnitude of any one component of the radiative surface heat budget, probably in large part because of poor knowledge of FCC. More success has been made in estimating net surface heat budgets, because of the offsetting effects of clouds on surface energy exchange. However, if the predicted energy exchange is smaller than in reality, then the predicted weather will be weaker than reality. Determining the magnitude of each of the components of the heat budget is therefore important not only for understanding the climate but also for accurately depicting the weather over Antarctica.

This paper provides estimates of some key parameters of the Antarctic atmosphere. Measurements of broadband and spectral longwave downwelling radiative fluxes made at the South Pole Station during 2001 are presented. These longwave fluxes dominate the surface heat budget in Antarctica because of the region's high solar albedo and prolonged periods of darkness. We partition the spectral infrared fluxes into a few bands so that the importance of different gases and spectral regions to the downwelling radiative flux can be assessed. FCC is determined objectively based on both broadband and spectral infrared measurements and then compared with visual observations. The FCC is utilized together with measured radiation fluxes to determine longwave, downwelling, clear-sky fluxes (LDF_{clear}) and longwave downwelling cloud radiative forcing (LDCRF).

Acronyms used in this paper are given in Tables 1 and 2.

2. Instrumentation and data

The data used in this study come from several sources: (a) the South Pole Atmospheric Radiation and Cloud Lidar Experiment (SPARCLE), performed from January to October 2001 (Walden et al. 2001); (b)

TABLE 2. Acronyms of terms used in text.

Acronym	Definition
AERI	Atmospheric Emitted Radiance Interferometer
APP-x	AVHRR Polar Pathfinder
ARM	Atmospheric Radiation Measurement
AVHRR	Advanced Very High Resolution Radiometer
CAS	Clean Air Sector
CMDL	Climate Monitoring and Diagnostics Laboratory
FTIR	Fourier Transform Infrared Interferometer
IR	Infrared
ISCCP	International Satellite Cloud Climatology Project
PAERI	Polar Atmospheric Emitted Radiance Interferometer
SPARCLE	South Pole Atmospheric Radiation and Cloud Lidar Experiment
SPMO	South Pole Meteorology Office
UARS	*Upper Atmospheric Research Satellite*

a field experiment performed at the South Pole in 1992 (Walden 1995; Walden et al. 1998); (c) routine measurements of temperature and atmospheric composition made by the Climate Monitoring and Diagnostics Laboratory (CMDL) of the National Oceanic and Atmospheric Administration (NOAA) at the South Pole during 2001; and (d) the routine visual cloud observations made by the South Pole Meteorology Office (SPMO) during 2001.

All uncertainties in the data presented here are listed in Table 3.

a. Polar Atmospheric Emitted Radiance Interferometer

One primary objective of SPARCLE was to characterize the downwelling longwave radiation spectrum over the South Pole. Downwelling infrared spectra were measured with the Polar Atmospheric Emitted Radiance Interferometer (Polar AERI, or PAERI). A brief, general description of the PAERI is given below. More information on AERI instruments is given by Knuteson et al. (2004a,b).

The PAERI viewed the sky at several angles during each day of operation. The instrument was operated inside an insulated shelter with thermostatically controlled heaters. It was deployed on the border of the "Clean Air Sector" (CAS) upwind of South Pole Station, and viewed out over the CAS. The CAS has borders parallel to 0° and 110° E longitude. Prevailing winds come from between 0° and 90° such that views into the CAS are of a pristine environment. The PAERI field-of-view (FOV) half-angle of 23 mrad was pointed in a direction parallel to 20°E, and regularly viewed at least three zenith angles. Figure 1 indicates the routine zenith angles observed by the PAERI each month. Each angle was observed for about 1.5 min with a repeat time of approximately 10 min, yielding about 240 spectra each day.

Quality control procedures were implemented to reject data contaminated by frost-covered mirrors, attenuation of the instrument signal because of blowing snow, unstable instrument temperatures, and direct sunlight. Approximately 20%–25% of spectra were eliminated each day by the quality-control procedures. About 1800 spectra remained suitable for analysis at each angle for each month. During some months, such as January 2001, the PAERI was used for additional tasks other than observing downwelling radiances at routine viewing angles. In the most extreme case, this reduced the total number of spectra to about 1000 spectra per angle per month, excluding the time period from 14 March to 27 April 2001 when the PAERI was not operating. By comparison to routine visual cloud observations, which are taken only four times per day, this

TABLE 3. Description of instrumentation and uncertainties associated with each measurement or calculation. The uncertainties for the CMDL 2- and 22-m temperatures (T_2 and T_{22}) are from Hudson and Brandt (2005). The O_3 uncertainties are for the surface and are from B. Johnson (2004, personal communication). The two uncertainties in the LBLRTM LDF_{clear} are from varying the temperature and humidity profiles, respectively, by one standard deviation. (All uncertainties quoted in this paper are one standard deviation unless stated otherwise.)

Instrument	Experiment	Uncertainty (1σ)	Range of sensitivity
PAERI	SPARCLE	1 RU	450–1800 cm^{-1}
FTIR	Walden (1995)	1–3 RU	550–1667 cm^{-1}
RS80 P	CMDL	0.5 hPa	1060 to 3 hPa
RS80 T	CMDL	0.2 K	183 to 333 K
RS80 RH_w	CMDL	3% RH_w	0%–100%
RS80 O_3	CMDL	4 ppbv	0–450 ppbv
T_2, T_{22}	CMDL	0.1 K	−85° to 50°C
Pyrgeometer	CMDL and Walden (1995)	8 W m^{-2}	200–2500 cm^{-1}
LBLRTM LDF_{clear}	Atmospheric and Environmental Research	1, 0.5 W m^{-2}	1–2500 cm^{-1}
PAERI LDF_{clear}	SPARCLE	0.25 W m^{-2}	450–1800 cm^{-1}

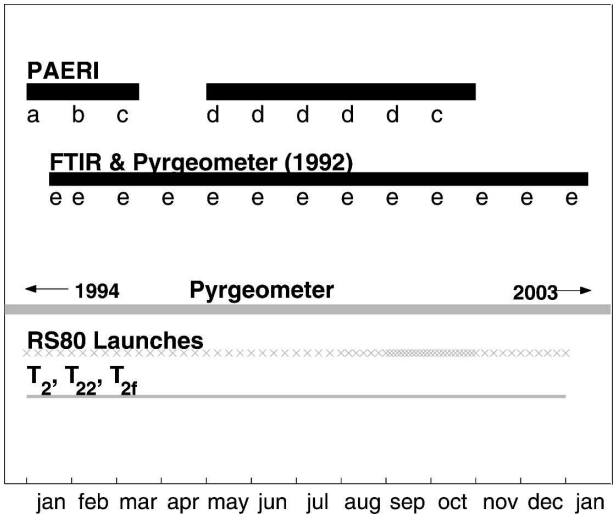

FIG. 1. Timelines of data used in this study. All data were collected during 2001 except for the Fourier Transform Interferometer (FTIR) and pyrgeometer data collected during 1992 (Walden 1995). The black lines indicate data collected by us; the gray lines indicate data collected by NOAA's CMDL. The Xs indicate RS80 launch dates. During the southern austral spring, CMDL launched 8–12 sondes per month. The 2- and 22-m temperature and 2-m frost point temperature are represented as T_2, T_{22}, and T_{2f}, respectively. The set of zenith angles viewed are (a) 0°, 60°, 75°, 78°; (b) 0°, 45°, 50°, 60°, 75°, 78°; (c) 0°, 50°, 70°; (d) 0°, 60°, 78°; and (e) 45°, 60°, 75°. Here (e) applies only to the FTIR; the pyrgeometer has a hemispheric FOV.

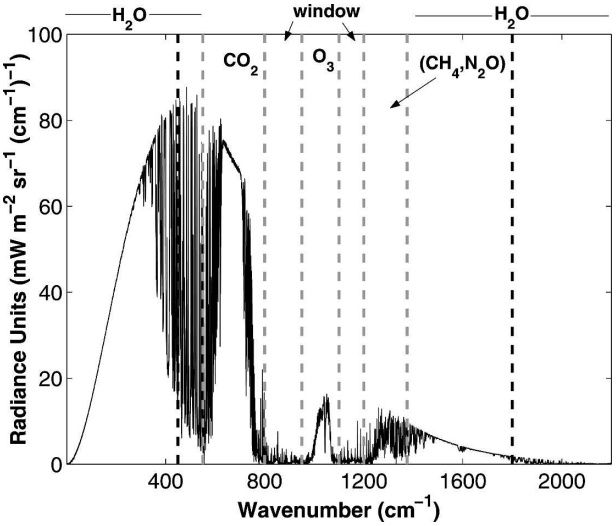

FIG. 2. Clear-sky spectrum of downwelling infrared radiance as modeled by LBLRTM for Jan 2001 over the South Pole. (See section 3a for a discussion of LBLRTM.) The PAERI passively observes infrared radiances from 450 to 1800 cm^{-1} (5.5 to 22 μm) with an unapodized resolution of 0.48 cm^{-1}. [Apodization is described in Bell (1972).] The radiances are reported in units of mW m^{-2} sr^{-1} $(cm^{-1})^{-1}$, which is called a radiance unit (RU) in this study. Table 3 contains a summary of uncertainties in the PAERI radiances and derived fluxes. The black vertical dashed lines denote the spectral limits of the PAERI. The gray dashed lines separate the spectrum into emission bands based on the primary gaseous emitter in each region, as listed at the top of the figure. See Table 6 for exact bandwidths of the emission bands.

is a sufficient number of spectra to adequately characterize the monthly mean FCC, the downwelling radiance under clear skies, and the monthly mean LDCRF. The issue of adequate sampling is addressed further in sections 4 and 5. Figure 1 gives the seasonal coverage of all the data used in this study.

Figure 2 shows a clear-sky, summertime, downwelling infrared spectrum over the South Pole modeled using the line-by-line radiative transfer model (LBLRTM). (This model is discussed in section 3a.) The black vertical dashed lines show the spectral bandwidth of the PAERI, and the gray vertical dashed lines represent bands where different atmospheric gases emit. Figure 2 shows that CO_2 and H_2O are dominant contributors to the downwelling infrared radiation flux over east Antarctica and that clear-sky infrared radiation beyond the PAERI spectral bandwidth is dominated by emission from water vapor.

Clouds composed of ice and liquid water emit across the infrared spectrum like gray bodies of variable emissivity and temperature. The infrared emission from clouds depends mostly on the optical depth, FCC, and temperature of the clouds. To assess the accuracy and natural variability of the downwelling fluxes observed by the PAERI and pyrgeometer, the monthly mean fluxes, their standard deviations, and standard errors were computed (Table 4).

b. Pyrgeometer

The NOAA–CMDL pyrgeometer reports broadband longwave downwelling flux (LDF) with an accuracy of about 4 W m^{-2} under ideal operating conditions (E. G. Dutton 2004, personal communication). The operating procedures at the South Pole are identical to those described in Marty et al. (2003), who estimate the absolute accuracy of an Eppley pyrgeometer at 2 W m^{-2}. [Marty et al. (2003) is also a concise reference comparing both pyrgeometer broadband calibration and AERI spectral calibration to the common standard of LBLRTM.] We add an additional 6 W m^{-2} to this estimate of uncertainty due to errors induced by day-to-day operations, for a total uncertainty of 8 W m^{-2}. The conclusions of this work are not greatly affected by the uncertainties in individual pyrgeometer measurements because most of the results presented here are monthly averages.

The spectral bandwidth of the pyrgeometer is about 4–50 μm. It has a temperature-dependent calibration

TABLE 4. Monthly means, and standard deviations (std dev) and standard errors (SEs) of the monthly means of downwelling flux measured by the PAERI and pyrgeometer under all conditions and under clear conditions during 2001. The time series of LDF_{clear} (column 4 mean) is shown in Fig. 8 for broadband and partial band, and the time series of LDCRF (column 3 mean minus column 4 mean) is shown in Fig. 10. All entries below are in W m^{-2}.

	$PAERI_{all}$			$PAERI_{clear}$			$Pyrgeometer_{all}$ (LDF_{all})			$Pyrgeometer_{clear}$ (LDF_{clear})		
Month	Mean	Std dev	SE	Mean	Std dev	SE	Mean	Std dev	SE	Mean	Std dev	SE
Jan	94.3	28.7	2.2	59.4	5.7	0.3	140	26.0	0.1	126	6.2	0.3
Feb	79.3	30.3	0.7	53.6	6.7	0.2	137	30.0	0.2	114	7.5	0.3
Mar	60.4	28.5	1.0	39.6	6.2	0.3	107	27.7	0.1	89	7.9	0.4
Apr							95	20.1	0.1			
May	56.8	21.4	0.5	36.2	4.7	0.2	102	30.4	0.2	73	14.3	0.5
Jun	55.9	21.6	0.6	35.9	4.2	0.2	99	24.6	0.1	77	4.8	0.3
Jul	48.0	15.9	0.3	33.6	5.9	0.2	90	19.0	0.1	74	9.4	0.3
Aug	41.6	16.8	0.4	30.0	4.0	0.1	85	24.6	0.2	66	5.1	0.2
Sep	58.1	22.9	0.5	36.9	6.3	0.2	103	35.4	0.2	76	21.7	0.8
Oct	46.2	18.7	0.4	36.6	5.1	0.2	94	29.9	0.1	78	16.1	0.5
Nov							129	30.1	0.2			
Dec							133	31.0	0.2			

that compensates for out-of-band fluxes due to emission from the water vapor rotational band so that its effective bandwidth extends to much longer wavelengths. It was calibrated in June 1999 and again in February 2004 with no significant drift in its calibration. The pyrgeometer remained unshaded during times of daylight, which can lead to, on average, an additional 3 W m^{-2} in downwelling irradiance at midlatitudes (Philipona et al. 2001). This effect is likely to be smaller at the South Pole and only affects data taken during summer (December and January) due to the low maximum solar elevation at 90°S.

The temperature dependence of the instrument sensitivity was tested down to −40°C with no significant deviation from the reference standards. Near-surface temperatures at the South Pole get much lower than this, which calls into question the estimate of the water vapor rotational band emission using CMDL's temperature-dependent calibration. However, even at Antarctic winter temperatures, the part of the rotational band outside the pyrgeometer's spectral bandwidth is almost completely saturated, so the calibration should be fairly accurate. More information on the CMDL pyrgeometer calibration can be found in Dutton (1993). As indicated in Fig. 1, the pyrgeometer (an Eppley PIR) operated continuously throughout the 2001 field season. Figure 3 is a histogram of downwelling fluxes from the pyrgeometer during January 2001. Most months display a similarly skewed distribution due to the radiative equilibrium between the surface and the atmosphere reached under clear skies.

c. Atmospheric profiles

Profiles of atmospheric temperature and gaseous composition are needed for the radiative transfer calculations described below. Profiles of temperature (T), relative humidity with respect to water (RH_w) and ozone concentration were obtained by CMDL using Vaisala's RS80H radiosondes. For most of the year, CMDL launched four balloons each month. However, during periods when dramatic changes in the stratospheric ozone layer were expected, CMDL launched as

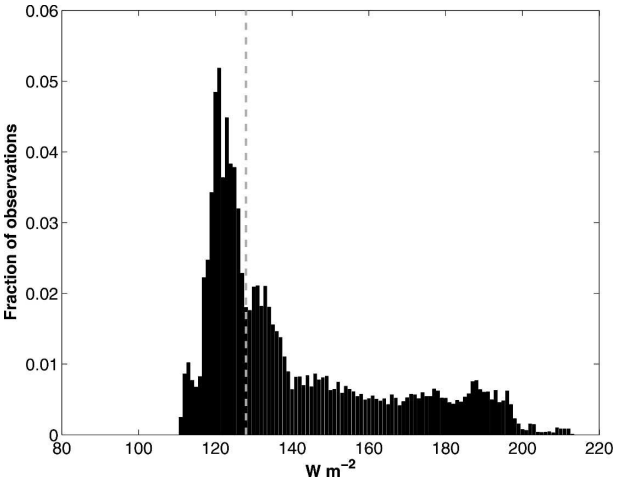

FIG. 3. Histogram of pyrgeometer measurements for Jan 2001. The vertical dashed line is the clear/cloudy threshold, explained in section 3b. The largest peak is due to clear-sky observations, while the long tail toward higher fluxes is due to clouds of variable coverage, optical thickness, and temperature. The clear-sky thresholds (different for each month) are derived from LBLRTM simulations based on monthly mean atmospheric profiles. Ideally these profiles would be climatological profiles and could be used operationally, but historical radiosonde humidity measurements over Antarctica are not accurate enough for this purpose. The clear-sky thresholds used here are based only on monthly mean atmospheric profiles from 2001. Bin size = 1 W m^{-2}. The number of measurements is 44 432.

many as 12 balloons each month. The launch dates for 2001 are shown in Fig. 1.

Monthly mean profiles of T, RH_w, and O_3 were computed for 2001 from the CMDL radiosondes. The humidity profiles were corrected for lag in the humidity sensors in a manner similar to the way temperature profiles were corrected by Mahesh et al. (1997). The radiosonde profiles were also corrected for errors in observed humidity and pressure induced by thermal shock during the launch. Thermal shock errors in Vaisala's RS80s are described by Hudson et al. (2004). It was discovered during the course of this study that those errors are greatly reduced when the radiosonde is ventilated by flight. For modeling purposes, the atmospheric profiles from the RS80 launches were interpolated to a grid of altitudes that is finely spaced near the surface and becomes gradually coarser with altitude.

The CMDL radiosonde profiles were supplemented near the surface with temperatures at 2 and 22 m (T_2, T_{22}) and frost point temperatures at 2 m (T_{2f}), which were collected by CMDL on a tower located on the border of the Clean Air Sector. For the upper atmosphere, between ~30 and 60 km, profiles of T, H_2O, and O_3 were obtained from the *Upper Atmosphere Research Satellite* (*UARS*) dataset for the south polar region (Walden et al. 1998). Other trace greenhouse gas concentrations were estimated from climatological values. Values of N_2O and CH_4 come from Houghton et al. (2001), while values for CCl_4, CFC_{11}, and CFC_{12} come from Walden et al. (1998). Table 3 gives the uncertainties associated with the atmospheric profiles. Uncertainties in the *UARS* data are discussed by Walden et al. (1998).

d. The 1992 data

An additional dataset was collected from January 1992 to January 1993 (Walden 1995; Walden et al. 1998), including downwelling infrared spectra at three angles (45°, 60°, and 75°), and downwelling broadband irradiances. Infrared spectra were collected at 12-h intervals, yielding 510 spectra for analysis after quality control. The spectral mean uncertainty of the 1992 radiance measurements is from 1 to 3 radiance units (RUs), and the uncertainty of the 1992 pyrgeometer measurements is also set to 8 W m^{-2} (Table 3). Further details regarding the 1992 experiment can be found in Walden (1995) and Walden et al. (1998).

e. South Pole Meteorology Office

The South Pole Meteorology Office (SPMO) reported visual observations of FCC every 6 h for the entire year. From these we calculated monthly mean FCC amounts. All "sky-obscured" observations were classified as overcast because such reports almost always occurred during times of blowing snow. Our own visual observations indicate that blowing snow is almost always accompanied by clouds overhead. These observations are substantiated by photomicroscopy of ice crystals done at the South Pole during 1992 (Walden et al. 2003), which found falling snow grains along with blowing snow crystals in all blowing snow events. The uncertainty for FCC_{vis} is ±4%. This is based on a statistical study of Warren et al. (1986), which involves subsampling of a large dataset to determine the error in monthly mean cloud cover as a function of the number of observations.

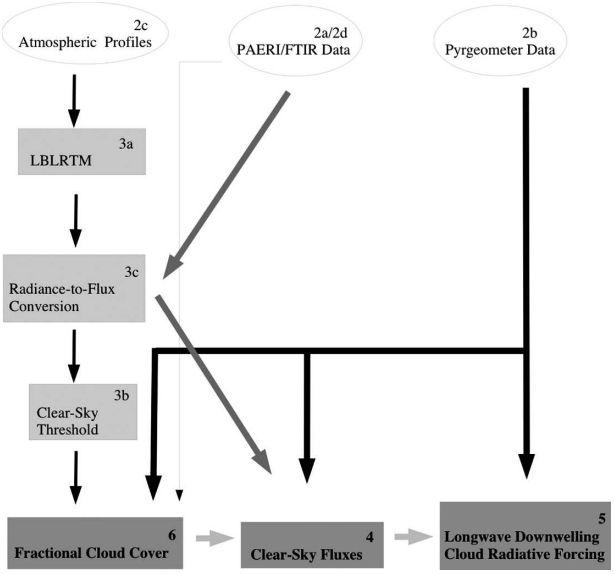

FIG. 4. Flow diagram of analysis procedures. The white ovals designate datasets; processing models and methods are in light gray rectangles; the resulting data products are in dark gray rectangles. The number in the upper right corner of each box denotes the relevant section of the paper.

3. Models and methods

The three data products, LDF_{clear}, LDCRF, and FCC, (discussed in sections 4, 5, and 6, respectively) require various data analysis steps to produce. These processing steps are illustrated in Fig. 4 and are described below.

a. Line-by-line radiative transfer model

The line-by-line radiative transfer model (LBLRTM), developed by Atmospheric and Environmental Re-

search (Clough et al. 1992; Clough and Iacono 1995), was used to simulate clear-sky downwelling infrared radiances. These simulations were based on the monthly mean atmospheric profiles described above. Monochromatic radiances were modeled for zenith angles of 0°, 30°, 60°, and 78°, and then convolved with the instrument response function of the PAERI to degrade the spectral resolution to that of the PAERI. The resulting radiances were used to calculate LDF values over the South Pole. The procedure for determining broadband and partial-band LDF from spectral radiances is described in section 3c. The modeled downwelling radiances and fluxes are used to determine FCC from the PAERI and pyrgeometer data (section 3b). The modeled LDF_{clear} is also used to explain the relative contributions of H_2O and CO_2 to the clear-sky flux, discussed in section 4.

Errors in the fluxes calculated by LBLRTM are estimated by comparing LBLRTM model runs using the atmospheric profiles described in section 2c with model runs made using perturbed atmospheric profiles. Both the temperature and humidity profiles are perturbed separately by the RS80 uncertainties reported by Vaisala (1997); ±0.2 K in temperature and ±3% in RH_w. The error induced in the model calculation of LDF due to a uniform 0.2-K increase in tropospheric temperatures, applied to the monthly mean January 2001 atmospheric profile, is +1 W m^{-2}, and that induced by a 3% increase of tropospheric RH_w is +0.5 W m^{-2} (Table 3). The combined error is slightly less than the sum of the two errors.

Errors in the LBLRTM simulations due to errors in the line shape parameters are discussed by Rowe (2004) and Tobin et al. (1999). Those studies are focused on regions of water vapor emission but are useful for perspective on the maximum spectral errors in the LBLRTM algorithm due to the present state of knowledge of spectral line shapes.

b. Clear-sky thresholds derived from infrared radiation measurements

Since cloud cover from visual observations is unreliable during the polar night it was necessary to develop methods of determining FCC from our radiation measurements. Both the pyrgeometer and the PAERI are sensitive to variations in infrared radiation that accompany changes in cloud cover.

Monthly theoretical clear-sky thresholds were developed for the purpose of identifying clear skies from the radiation measurements. The thresholds are similar in principle to other clear-sky indices developed for downwelling infrared data. Marty and Philipona (2000) used a clear-sky index that is a broadband atmospheric emissivity threshold based on near-surface temperature and humidity measurements. They showed that their index was quite consistent with the visual synoptic observations despite having only seasonal clear-sky parameterizations of broadband atmospheric emissivity for summer and winter. Further analysis in Sutter et al. (2004) shows that while the technique of Marty and Philipona (2000) has some success, it overestimates FCC under strong inversions and is unable to distinguish high thin clouds from clear skies. This relative failure under inversion conditions is due to their parameterization of the emissivity of the entire atmosphere in terms of near-surface properties alone. The clear-sky thresholds presented here are based on atmospheric profiles of temperature and humidity, so they should be more reliable.

1) PYRGEOMETER

The theoretical clear-sky thresholds applied to the pyrgeometer data were determined from LBLRTM simulations of LDF_{clear} for each month of 2001. Downwelling radiances were modeled at four different zenith angles (0°, 30°, 60°, and 78°) and converted to broadband LDF_{clear} via the procedure outlined in section 3c. An additional irradiance increment was added to the simulated LDF_{clear} to account for the effects of diamond dust. This increment was estimated by assuming an approximate value for the emissivity of a diamond-dust layer over the South Pole ($\varepsilon = 0.05$) and fitting a blackbody curve scaled by the emissivity to the window region of clear-sky PAERI spectra. The estimated window radiances were then converted to fluxes. For January, a diamond-dust temperature of 250 K provided a good fit to the radiances in the window region. For February, March, and October a temperature of 235 K sufficiently fit the clear-sky radiances in the window region. A typical winter diamond dust cloud was simulated with a temperature of 220 K.

The LDF_{clear} from monthly LBLRTM simulations, augmented by the seasonal radiative effects of diamond dust, is our monthly, clear-sky threshold for the pyrgeometer data. All LDF values below the threshold were classified as clear, while all LDF values higher than the threshold were classified as cloudy (Fig. 3). A binary, minute-by-minute clear/cloudy time series was produced. Monthly mean FCC was then calculated from the binary time series of cloud detection. It is assumed that for the monthly mean the pyrgeometer cloud detection frequency will equal FCC and is thus referred to as FCC_{pyr}. The resulting monthly mean values of FCC_{pyr} for 2001 are discussed in section 6. Adding or

subtracting the irradiance of another diamond-dust layer to or from the clear-sky threshold caused the monthly FCC_{pyr} to change by an absolute amount of 2%–3% (Table 5).

The calculated thresholds for November and December 2001 based on the November and December LBLRTM profiles seemed to be low when compared with the thresholds from February and January, respectively. These months were compared because they have similar near-surface temperatures (Warren 1996). We suspect that the monthly mean profiles used to calculated the November and December thresholds are unrepresentative of those months. An independent method for determining FCC from pyrgeometer measurements described in Town et al. (2005) confirms that the original November and December clear-sky thresholds are too low.

A weakness of this algorithm is that it is susceptible to mistaking scattered, thin, or cold clouds as clear skies. It is not certain by how much FCC_{pyr} underestimates the actual FCC due to this miscategorization. This is assessed by comparison with other methods of determining FCC in section 6.

2) PAERI

The theoretical threshold used to derive FCC from the PAERI data (FCC_{PAERI}) is based on a method analogous to that just described for the pyrgeometer. A radiance ratio (RR) was computed and used as a test for clear skies for each zenith-looking spectrum collected during 2001:

$$\mathrm{RR} = \frac{\int_{450}^{1800} L_{\mathrm{obs}}(\upsilon)\, d\upsilon}{\int_{450}^{1800} L_{\mathrm{bb}}(\upsilon)\, d\upsilon}. \quad (1)$$

The numerator is simply the sum of PAERI radiances from 450 to 1800 cm^{-1}. The denominator was determined by taking the mean brightness temperature (T_b) between 630 and 640 cm^{-1} and computing the blackbody spectrum of T_b for the spectral range 450–1800 cm^{-1}. An example of the blackbody curve employed is shown in Fig. 5. The mean brightness temperature between 630 and 640 cm^{-1} is used because it usually represents emission from the inversion top, typically the warmest part of the troposphere over the South Pole. Therefore, normalizing by the mean brightness temperature of 630–640 cm^{-1} limits the RR maximum to be approximately 1.0. A histogram of RRs for January 2001 is shown in Fig. 6.

To use the RR for the purpose of determining FCC_{PAERI}, zenith-looking spectral radiances were computed for each month with LBLRTM, using the mean atmospheric profiles described in section 2c. The simulated spectra were computed with the same spectral limits and resolution as the PAERI observations. The radiative effects of diamond dust were added to the window region to simulate a zenith-looking, clear-sky-with-diamond-dust spectrum for each month. An RR was then computed for each monthly simulation. This clear-sky RR (CSR) was used to calculate another binary clear/cloudy time series. Monthly mean FCC_{PAERI} values were calculated through time averaging of the binary time series from the PAERI measurements.

It is clear from Fig. 6 that there is a definite lower limit to the day-to-day RR that occurs under clear skies. The vertical line indicates the computed CSR threshold

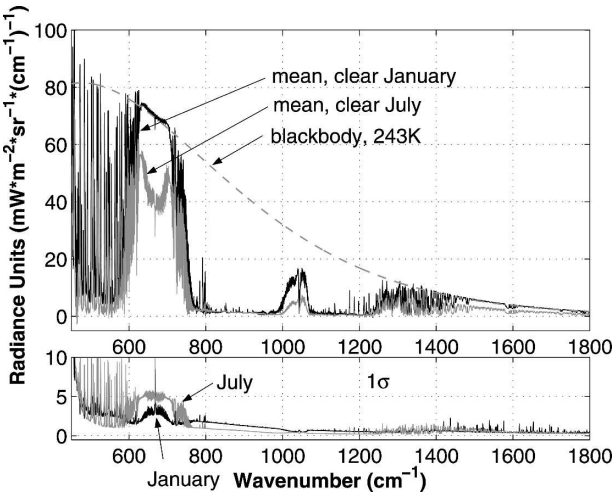

FIG. 5. Longwave downwelling atmospheric spectra at South Pole. (top) Solid lines are mean, zenith-looking, clear-sky spectra for Jan and Jul 2001. The dashed line represents a blackbody radiance spectrum at 243 K (the significance of which is described in section 3b). (bottom) One standard deviation (1σ) about the means for Jan and Jul 2001, in RU.

TABLE 5. Table of confidence in cloud cover estimates. The first two rows are sensitivities of FCC_{pyr} and FCC_{PAERI} to the addition/subtraction of the radiative effects of a single layer of diamond dust to/from the clear-sky threshold. The third row contains the uncertainty in FCC_{vis} based on rms error in average cloud cover over land [Fig. 5 of Warren et al. (1986)] for the mean number of observations each month. This value of 4% is based on just the sampling error; biases can be much greater during the winter night.

FCC_{pyr}	±3%
FCC_{PAERI}	−10/+18%
FCC_{vis}	±4%

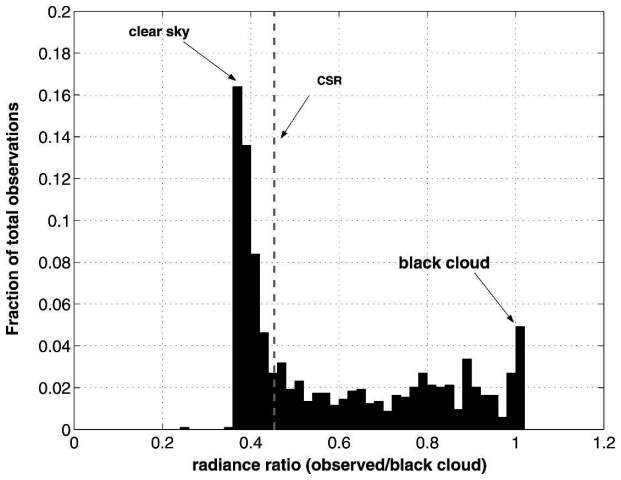

FIG. 6. Histogram of PAERI radiance ratios (RRs) for Jan 2001. Dashed vertical line represents the clear-sky-ratio threshold described in section 3b. The RR is usually between about 0.35 and 1.0, depending on atmospheric temperature and humidity, and the optical depth and temperature of any clouds overhead. Bin size is 0.02. The total number of RRs is 1037.

for January 2001. Any zenith-looking spectrum with an RR below the monthly CSR is classified as clear; the others are cloudy. Also labeled on Fig. 6 is the special case of a "black" cloud. This value, RR = 1.0, is obtained when the cloud overhead is optically thick and the atmosphere below the cloud has the same temperature as the cloud. A time series of zenith-looking PAERI spectra is then used for determining FCC_{PAERI}.

FCC_{PAERI} was ultimately used to categorize the downwelling flux data as clear or cloudy because it was deemed to have the fewest a priori weaknesses. The radiance ratio method is far less susceptible to mistaking scattered clouds for clear skies than is the pyrgeometer method, because of the narrow FOV of the PAERI. It is also much less susceptible to mistaking thin or cold clouds for clear skies since the method is very sensitive to relative changes in the window region (800–1200 cm^{-1}) and "dirty window" (450–550 cm^{-1}) rather than absolute changes in total PAERI-band irradiance. In addition, the process of summing across the entire spectrum and dividing by a blackbody radiance that is specific to the spectrum in question minimizes any uniform biases in the PAERI spectrum.

The monthly means of FCC_{PAERI} have been adjusted to include cloudy times when the PAERI was not operating. Such times were typically easy to assign visually as cloudy since they mainly occurred during spells of blowing snow. As discussed above, it appears that blowing snow is almost always accompanied by clouds at the South Pole. In any case, the effect of blowing snow on LDF is quite similar to that of clouds. Adjustments to monthly mean values of FCC_{PAERI} were as much as +12%, but were typically closer to +5%.

Table 5 shows that adding or subtracting the radiative effects of a layer of diamond dust to the CSR causes FCC_{PAERI} to decrease by 10% or increase by 18%, respectively.

Monthly means of FCC_{PAERI} for other routinely observed zenith angles were also calculated to assess the effect of cloud thickness on FCC_{PAERI}. Compared to the zenith value, monthly FCC_{PAERI} increased by only 1% at a zenith angle of 60° and 2% at an angle of 78°. This small effect is a result of two climatic factors at the South Pole. First, the clouds are predominantly thin throughout the year, so viewing the sides of clouds does not increase FCC significantly. Second, daytime visual observations indicate that 74% of the time the sky is within one octa of being clear or cloudy. Thus, even an instrument with as narrow an FOV as the PAERI would not get much opportunity to see sides of clouds.

c. *Radiance-to-flux conversion (integration over angle and wavenumber)*

The monthly mean spectral radiances for the routinely observed angles were used to calculate monthly mean partial-band LDF by the following method (illustrated in Fig. 7). The monthly mean, clear-sky, PAERI band (i.e., 450–1800 cm^{-1}) and partial-band radiances (such as shown in Fig. 5) were summed over wavenumber and plotted as functions of the cosine (μ) of the

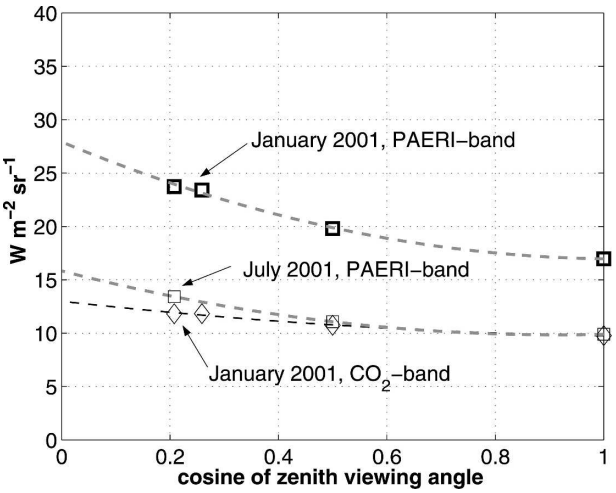

FIG. 7. Clear-sky PAERI-band radiances (□) for Jan and Jul 2001 as a function of the cosine of the zenith angle. Also shown are the clear-sky CO_2-band radiances for Jan 2001 (◊). The dashed lines represent quadratic functions that were fit to each of the datasets to convert PAERI-band radiances to fluxes via Eq. (2).

TABLE 6. Bandwidth limits for analysis of spectral infrared data in cm^{-1} and μm.

Absorbing gases	Bandwidth (cm^{-1})	Bandwidth (μm)
Water vapor (H_2O)	20–550, 1375–2500	18–500, 4–7.3
Carbon dioxide (CO_2)	550–800	12.5–18
Ozone (O_3)	950–1100	9.1–10.5
Window region	800–950, 1100–1200	10.5–12.5, 8.3–9.1
Methane/nitrous oxide (CH_4/N_2O)	1200–1375	7.3–8.3

zenith angle (θ). A quadratic curve was fit to the points, which was then integrated over μ to yield the monthly mean LDF_{clear} (Fig. 7):

$$LDF_{PAERI} = \int_{450}^{1800} \int_{0}^{2\pi} \int_{0}^{1} L_{PAERI}(\upsilon, \mu)\mu \, d\mu \, d\phi \, d\upsilon, \quad (2)$$

L_{PAERI} is the PAERI radiance at a particular wavenumber (υ) and ϕ is the azimuthal angle; azimuthal symmetry is assumed here.

The partial-band LDF_{clear} values were calculated using the spectral limits shown in Fig. 2 and the μ dependence shown in Fig. 7. The partial-band LDF_{clear} due to water vapor rotational and vibrational emission deserves a more detailed explanation. As stated earlier, we assume that all significant clear-sky atmospheric infrared radiation outside the spectral bandwidth of the PAERI was due to emission from water vapor. This assumption was confirmed by LBLRTM calculations. To calculate the monthly mean LDF_{clear} due to emission from water vapor, the monthly mean LDF_{clear} for the entire PAERI bandwidth is subtracted from the monthly mean broadband LDF_{clear} from the pyrgeometer. Then the monthly mean LDF_{clear} for the spectral regions 450–550 and 1375–1800 cm^{-1} are added to the out-of-band water vapor emission resulting in the total LDF_{clear} from water vapor:

$$LDF_{H_2O} = LDF - LDF_{PAERI} + LDF_{450–550} + LDF_{1375–1800}. \quad (3)$$

Since LDF_{H_2O} in Eq. (3) is calculated from two different measurements, it is affected by the biases and uncertainties of both instruments.

It is interesting that in January, the CO_2-band LDF_{clear} is as large as the entire PAERI-band LDF_{clear} for July (Fig. 7). The nearly flat curve fit to the January, CO_2-band LDF_{clear} highlights the fact that the boundary layer is nearly isothermal during January (i.e., the PAERI observed almost equal radiances at all angles). Thus, most of the curvature in the January PAERI-band radiances in the upper curve in Fig. 7 is due to the stratification of water vapor in the lower troposphere. See Mahesh et al. (2001a) for a discussion of CO_2 infrared *e*-folding distances over the South Pole.

4. Clear-sky fluxes

To quantify the greenhouse effect of the various gases in the atmosphere, the infrared spectrum was separated into bands based on the gas or gases most responsible for the emission within a given spectral region. The spectral band limits used here are summarized in Table 6 and Fig. 2.

The broadband and partial-band LDF_{clear} are plotted as functions of month in Fig. 8 and listed by season in Table 7. The seasonal cycles of LDF_{clear} are similar for all gases. Water vapor and CO_2 are responsible for almost all the emission. The maximum LDF_{clear} values are observed during the short Antarctic summer when the lower troposphere is warmest and nearly isothermal. There is not a pronounced minimum in broadband LDF_{clear} during winter in Fig. 8; this is an illustration of the coreless winter described by Schwerdtfeger (1984).

Table 8 compares LDF_{all} values from different years, so as to place the field seasons in the context of the climatology of the South Pole. Both 1992 and 2001 are

TABLE 7. Seasonal LDF_{clear} from 1992 and 2001. The seasons on the Antarctic Plateau are traditionally defined as spring (Oct, Nov), summer (Dec, Jan), autumn (Feb, Mar), and winter (Apr–Sep) (Schwerdtfeger 1984). Units are W m^{-2}.

Band	Summer (Dec–Jan)	Autumn (Feb–Mar)	Winter (Apr–Sep)	Spring (Oct–Nov)
Broadband (1992)	119	99	79	94
Broadband (2001)	126	101	74	96
H_2O (2001)	83	66	48	63
CO_2 (2001)	35	29	23	28
O_3 (2001)	3	2	1	2
CH_4/N_2O (2001)	3	2	2	2
Window region (2001)	1	1	1	1

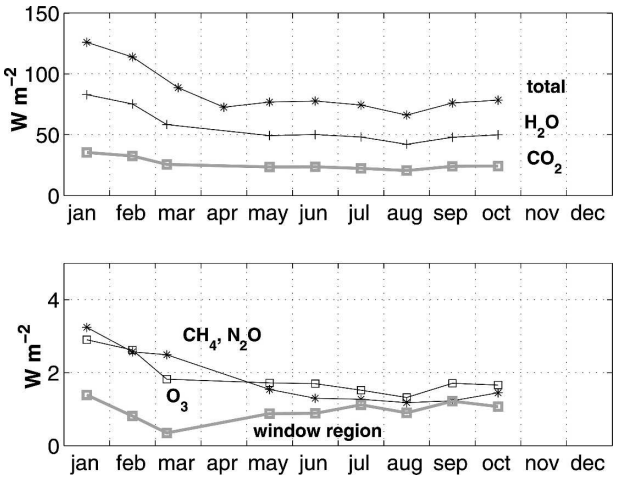

FIG. 8. Broadband and partial-band clear-sky, longwave downward flux (LDF_{clear}) for the South Pole in 2001. (See section 3c for a description of how the fluxes were determined.) The lower panel has an expanded vertical scale. Broadband and partial-band LDF_{clear} are calculated by integrating Eq. (2) over μ and across the spectral band limits described above. The existence of clear conditions was determined using both spectral and broadband IR data, using the methods described in section 3b. The tick marks denote the beginning and end of each month. The data points for Mar are not centered in the month because the PAERI was only operating during the early part of the month. There is no PAERI data for Apr.

within one standard deviation of the nine-year mean in Table 8. Both the 1992 and 2001 winters experienced less LDF_{all} than average, whereas the springs exhibit greater LDF_{all} than average. Nevertheless, the two years presented here are acceptably close to climatology to be considered normal.

LDF_{clear} values in the window region, due mainly to diamond dust, are seen to be very small in all months (Fig. 8). Emissions from O_3, N_2O, and CH_4 are also small. Water vapor contributes approximately two-thirds of the LDF_{clear} regardless of season while CO_2 contributes about one-third. The actual ratio of H_2O/CO_2 LDF_{clear} is in the range 2.1–2.3 throughout the year. This constancy is surprising because precipitable water vapor (PWV) decreases significantly from summer to winter, but atmospheric CO_2 concentration remains constant as the atmospheric temperatures drop dramatically.

a. Precipitable water vapor

It is relevant at this point to discuss the precise nature of the atmospheric water vapor cycle over the South Pole to fully address the puzzle of the H_2O/CO_2 flux ratio. Chamberlin (2001) estimated that the tropospheric PWV over the South Pole ranges from about 1.1 mm in summer to 0.4 mm in winter. His estimate was based on temperature soundings from 1961 to 1999 and the assumption that the entire troposphere is saturated with respect to ice. He also made an alternative estimate of PWV based on historical humidity soundings over the South Pole. Unfortunately, the hygristors used for those soundings are sluggish and inaccurate at low temperatures (Hudson et al. 2004).

Our estimates of the tropospheric PWV in 2001 (Fig. 9) are based on RS80 radiosonde soundings collected by CMDL, discussed in section 2c. The RS80s use significantly improved technology based on capacitance to determine humidity. Our PWV values for the summer are about 50% larger than Chamberlin's because the lower atmosphere is often saturated with respect to liquid water (and therefore supersaturated with respect to ice) during the summer. Indeed, other observations we have made using a video camera on a tethered balloon indicate that clouds of supercooled liquid droplets are common in summer, down to temperatures of −30°C or so.

Tropospheric ice saturation seems to be a valid assumption in the wintertime inversion layer; this explains why our estimates of PWV are similar to one of Chamberlin's estimates, which made this assumption. It is uncertain why Chamberlin's other estimate, based on inaccurate hygristor technology, is also similar. On average, about 70% of the PWV is below the altitude of 5 km above sea level (surface altitude at the South Pole is 2.835 km) (Fig. 9). During the 2001 winter, most of the atmospheric PWV was located in the 1-km layer centered at the top of the temperature inversion. Even though the near-surface atmosphere during winter is saturated with respect to ice, and often slightly supersaturated, this does not have a major effect on mean PWV amounts because of the low temperatures near the surface. Similarly, the atmospheric humidities above the inversion layer do not contribute much to PWV because the free troposphere is cold. During the summer, the mean RH_w of the atmosphere above the isothermal boundary layer is between 5% and 20% RH_w below ice saturation. During the winter the atmosphere above the inversion top is a more uniform 15% to 20% RH_w below ice saturation.

In summary, the atmospheric PWV varies from ~1.6 to 0.4 mm from summer to winter while the climatological mean surface temperature drops from −28° to −58°C (Warren 1996). The average PWV during summer is much higher than the clear-sky value (point X indicated in Fig. 9), as evidenced by the frequent occurrence of liquid water stratocumulus clouds.

TABLE 8. Broadband pyrgeometer measurements under all conditions in W m^{-2} for 1992, 2001, and 1994–2002. The standard deviations about the means are in parentheses.

Year	Summer (Dec–Jan)	Autumn (Feb–Mar)	Winter (Apr–Sep)	Spring (Oct–Nov)
1992	144 (29)	113 (21)	105 (33)	121 (29)
2001	138 (24)	121 (32)	96 (26)	113 (31)
1994–2002	140 (29)	118 (29)	114 (30)	98 (28)

b. *The relative contributions of H_2O and CO_2 to LDF_{clear}*

There are several factors to consider in explaining the seasonal cycle of the H_2O/CO_2 LDF_{clear} ratio. First, the shift of the blackbody spectrum with temperature puts more emphasis on the water vapor rotational band during winter than during summer. On the other hand, PWV decreases from summer to winter by over 50%. Other factors are the saturated nature of the 15-μm band of CO_2 and the variably saturated nature of the water vapor rotational band.

Because of the complex nature of these relationships we use LBLRTM to quantify these factors. Clear-sky profiles from summer and winter were input into LBLRTM to calculate downwelling infrared radiances at several angles. Values of LDF_{clear} from the water vapor and CO_2 bands were then calculated from the resulting radiances using the procedure outlined in section 3c. The profiles of T, water vapor mixing ratio, and pressure for the two cases were also permuted and input into LBLRTM to further investigate their relative importance.

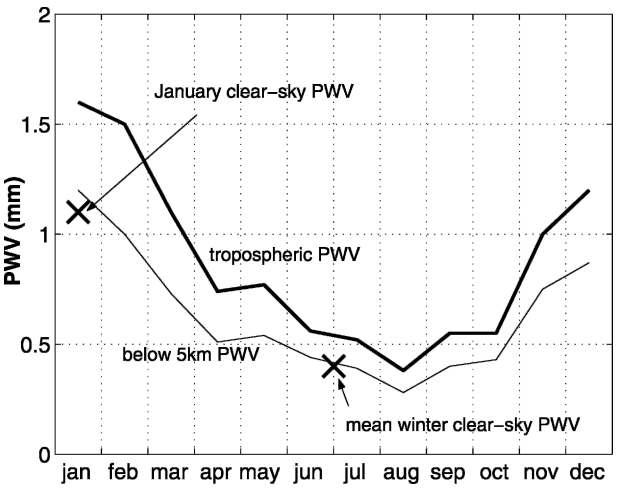

FIG. 9. Tropospheric precipitable water vapor for 2001 based on monthly mean RS80 soundings for all sky conditions. The Xs denote mean PWV amounts for clear-sky only, for Jan and for winter. A sensitivity study indicates that increasing RH_w by 3% increases PWV by ~0.06 mm during summer and ~0.03 mm during winter. Increasing temperature by 0.2 K throughout the troposphere, for fixed RH_w, results in an increase in PWV of 0.03 mm in summer and 0.01 mm in winter. Most of the PWV is below 5 km above sea level (thin line), i.e., within 2 km of the surface.

Table 9 shows the results of the permutations on the fluxes emitted by water vapor and CO_2. The LBLRTM results indicate that by decreasing the temperature, but not water vapor mixing ratio, from summer to winter values (row 1 to row 2 in Table 9) emission from the CO_2 band drops by a third, almost all the way to observed winter levels. However, water vapor emission decreases by only 23% (17 W m^{-2}).

In contrast, decreasing water vapor mixing ratio from summer to winter levels (row 1 to row 3 in Table 9) only decreases water vapor emission by 12 W m^{-2}. This is because the water vapor rotational band is already mostly saturated even at the low water vapor levels of winter. Emission in the CO_2 band is slightly reduced by the decrease in water vapor because there is some water vapor–CO_2 band overlap in the 550–600 cm^{-1} region.

Row 4 in Table 9 is presented for comparison to row 5 to illustrate that the decrease in atmospheric surface pressure from summer to winter has very little effect on LDF_{clear} or the flux ratio.

Thus, the temperature decrease from summer to winter is directly responsible for all of the decrease in the CO_2 emission but only approximately half of the decrease in the water vapor emission. The decrease in water vapor mixing ratio from summer to winter is responsible for the remaining decrease in water vapor emission. The constancy of the flux ratio can thus be seen as a consequence of the partial saturation of the water vapor bands, together with the reduced water vapor amount in winter.

Despite the accurate representation of Antarctic clear-sky downwelling radiances by LBLRTM in the past (Walden et al. 1998), there are still some discrepancies between our modeled and observed results. The modeled CO_2 LDF_{clear} in January is close to, but slightly greater than, the observed LDF_{clear} (row 1 of Table 9). Considering the fairly small uncertainties in both the PAERI observations and the LBLRTM simu-

TABLE 9. LBLRTM simulations of clear-sky fluxes due to water vapor and CO_2 emission based on clear-sky atmospheric profiles for Jan 2001 and for winter 2001 at the South Pole. The flux ratio is the flux from water vapor divided by the flux from CO_2, computed both from the model (Mod) and observations (Obs). The rows from top to bottom represent different LBLRTM simulations based on combinations of profiles of temperature, H_2O mixing ratio (MR), and pressure, from Jan and from winter. It was found that atmospheric pressure did not change sufficiently from summer to winter to affect LDF_{clear} significantly (row 4 vs row 5); it is only given here for the sake of completeness.

	CO_2 flux (W m^{-2})		H_2O flux (W m^{-2})		Flux ratio	
Conditions	Mod	Obs	Mod	Obs	Mod	Obs
Jan T, H_2O-MR, P	36.6	32.6	73.0	83.0	2.0	2.3
Jan H_2O-MR, P; winter T	24.7	—	56.4	—	2.2	—
Jan T, P; winter H_2O-MR	35.5	—	61.0	—	1.7	—
Jan P; winter T, H_2O-MR	23.8	—	50.1	—	2.1	—
Winter T, H_2O-MR, P	23.5	22.5	48.8	47.4	2.1	2.1

lations (Table 3) this difference is significant. The modeled LDF_{clear} from water vapor is less than the observed flux by almost 10 W m^{-2}, also a significant difference. However, during winter the modeled fluxes (row 5 of Table 9) agree quite well with observations. Taken together, the LBLRTM fluxes actually predict a slight increase in the H_2O/CO_2 flux ratio from 2.0 in summer to 2.1 in winter rather than the slight decrease that is observed. This is due primarily to a low modeled water vapor LDF_{clear} for summer, suggesting an inaccuracy in the model or an inaccurate representation of the atmosphere in the model.

It seems unlikely that model errors could cause the discrepancy. Walden et al. (1998) compared LBLRTM simulations of downwelling radiances based on atmospheric profiles similar to those described in section 2c to three clear-sky test cases from 1992. Their overall conclusion was that LBLRTM was able to accurately simulate downwelling radiances in the extreme climate of east Antarctica. The largest discrepancies between the simulations and observations occurred from uncertainty in the temperature and humidity profiles and uncertainties in the foreign-broadened continuum of water vapor. This study uses more accurate radiosonde soundings than those used in Walden et al. (1998), and also uses updated water vapor continuum coefficients in the LBLRTM simulation, so inaccuracies in the model results are not a likely explanation for the discrepancy between the modeled and observed H_2O/CO_2 LDF_{clear} ratios.

It is possible that the atmospheric humidity in this clear-sky January atmospheric profile (RH_w = 60%–70%) does not accurately represent the mean clear-sky humidity. We therefore increased tropospheric RH_w to 100% in LBLRTM with an otherwise normal January atmospheric profile to test the sensitivity of LBLRTM to dramatic changes in RH_w; LDF_{clear} was raised by only ~4.5 W m^{-2}.

A phenomenon that could explain these discrepancies is the presence of diamond dust under clear skies during summer and under all sky conditions during winter; diamond dust was not included in the LBLRTM calculations. The hypothesis is that LDF_{clear} emitted by water vapor lines in the boundary layer was absorbed by the near-surface ice crystals and spread across the entire infrared spectrum, including the gaps between the lines. Since the lower troposphere is nearly isothermal during summer at the South Pole, this results in an increase in LDF_{clear} in parts of the water vapor rotation band (as well as in other less strongly absorbed bands). The emission from diamond dust would not raise the CO_2-band fluxes by much because the CO_2 band is strongly absorbing.

In winter, however, the effect of diamond dust seems to be coincidentally canceled by the existence of the surface inversion. Most of the LDF_{clear} due to water vapor is from the top of the inversion layer. This downwelling emission is absorbed lower in the inversion layer by the ever-present diamond dust. The diamond dust again reemits the radiation across the entire infrared spectrum, as opposed to the spectral lines associated with gaseous emission, but this time it is emitting at a much lower temperature than the original emission temperature of the atmospheric water vapor. Thus, the strength of the clear-sky temperature inversion and the emission of the diamond dust apparently compensate to cause no net effect on the observed H_2O/CO_2 LDF_{clear} ratio in winter.

5. Longwave downwelling cloud radiative forcing

As used here, the longwave downwelling cloud radiative forcing (LDCRF) is the difference between all-sky downwelling flux and clear-sky downwelling flux:

$$LDCRF = LDF_{all} - LDF_{clear}. \quad (4)$$

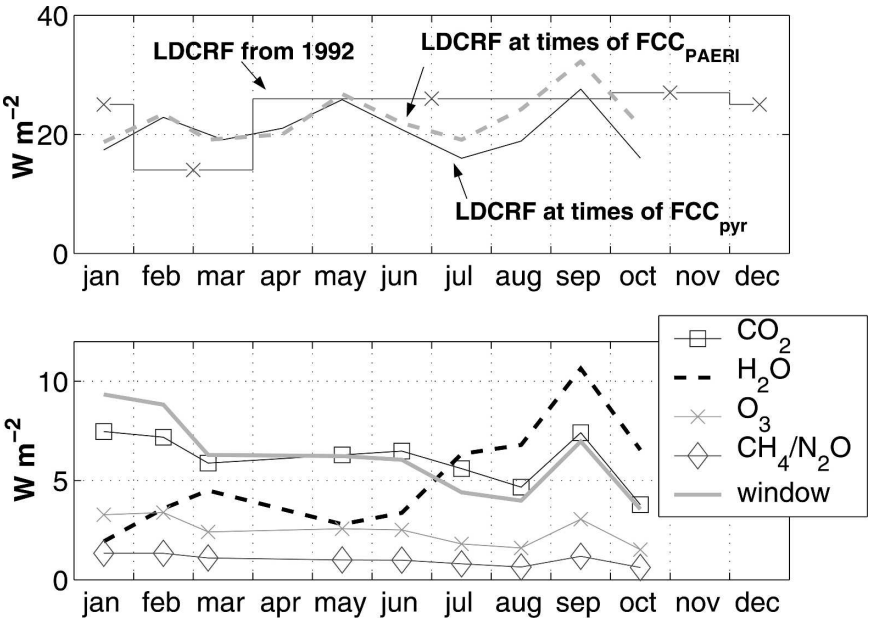

FIG. 10. Monthly values of (top) broadband and (bottom) partial-band longwave downwelling cloud radiative forcing for the South Pole during 2001. The seasonal values of broadband LDCRF for 1992 are also shown. In Mar, FCC_{PAERI} is available only for the beginning of the month. FCC_{PAERI} is not available for Apr.

(Some published work on longwave cloud radiative forcing at the surface reports instead the net forcing; i.e., downward minus upward, which we discuss later in this section.) These fluxes are computed for the broadband and the partial bands indicated in Fig. 2, including the window region, where LDCRF is typically large. From Eq. (4) it is clear that partly cloudy skies are included in the LDCRF calculation. This is similar to the definition of cloud radiative forcing at the top of the atmosphere in Ramanathan et al. (1989), except employed at the surface and only for terrestrial, downwelling radiation. Monthly LDCRF is the monthly mean LDF_{all} minus the monthly mean LDF_{clear}. Table 4 shows the monthly means of LDF_{all} and LDF_{clear}, their standard deviations and standard errors. Table 4 shows that most of the uncertainty in the LDCRF time series is due to natural variability in cloud cover rather than variability in LDF_{clear}.

Figure 10 shows the broadband and partial-band LDCRF for 2001, plus the seasonal values of broadband LDCRF for 1992. The top panel of Fig. 10 shows two broadband LDCRF calculations for 2001 and one for 1992. The thick dashed line is based on pyrgeometer measurements in 2001 for LDF filtered by FCC_{PAERI}. The thin curve is LDCRF from pyrgeometer measurements utilizing FCC_{pyr}.

The mean broadband LDCRF for 2001 is 20 or 23 W m^{-2} using the FCC_{pyr} or FCC_{PAERI} time series, respectively. The mean broadband LDCRF for 1992 is 24 W m^{-2}. The two estimates of broadband LDCRF for 2001 are consistent with each other despite being from slightly different time series. This lends weight to the representative nature of the PAERI time series.

The LDCRF derived here is compared with those of several other sites in Table 10. LDCRF at the South Pole is about half the global average even though the annual mean FCC for 2001 of 60% is nearly equal to the global annual mean FCC of 64% (Hahn et al. 1995). [In Table 10, 62% is quoted because it is the value used by Kiehl and Trenberth (1997) in their simulation.] This is because the low temperatures and humidities over the South Pole result in colder, optically thinner clouds than the global average. Clouds at the South Pole typically have optical depths less than 1 (Mahesh et al. 2001b).

Table 11 gives values of longwave net flux (LNF) and longwave net cloud radiative forcing (LNCRF) for various sites, including several estimates for the South Pole. During 2001 at the South Pole, LNCRF ranged from 14 to 6 W m^{-2} from summer to winter (not shown here). This was determined from observations of upwelling and downwelling fluxes taken by CMDL. The annual mean LNCRF for 2001 is 9 W m^{-2}. Pavolonis and Key (2003) determined annual mean surface LNCRF from the Advanced Very High Resolution Radiometer (AVHRR) Polar Pathfinder (APP-x) and International

TABLE 10. Comparison of LDCRF (W m^{-2}) at various sites: SPO = South Pole, Antarctica; BRW = Barrow, Alaska; SHEBA = Surface Heat Budget of the Arctic Ocean; BG = Bremgarten, Germany; FG = Feldberg, Germany; SGP = Southern Great Plains, United States; U-NSW = Uardry, New South Wales, Australia. Data on FCC are from Warren et al. (1986) and Hahn et al. (1995), except for South Pole, which is FCC_{PAERI}. The SHEBA LDCRF was determined from all-sky observations minus clear-sky calculations. The Global LDCRF was determined from clear and cloudy calculations, weighted by the FCC. Global LDCRF amounts to about 14% of LDF_{all} whereas LDCRF at the South Pole is approximately 19% of LDF_{all}.

Location	Lat, Lon	Alt (m)	Description	FCC (%)	LDCRF	Source
SPO (2001)	90°S	2835	Antarctic; mean (1 yr)	60	20	This work
SPO (1992)	90°S	2835	Antarctic; mean (1 yr)	—	24	This work
SHEBA	77°N, 165°W	0	Arctic; mean (1 yr)	—	37	Intrieri et al. (2002)
BRW	71.3°N, 156.6°W	0	Arctic; mean (1 yr)	59	44	Allan (2000)
BG	47.9°N, 7.6°E	212	Grassland; mean (4 yr)	68	43	Iziomon et al. (2003)
FG	47.9°N, 8°E	1489	Grassland; mean (4 yr)	68	38	Iziomon et al. (2003)
SGP	36.6°N, 97.5°W	315	Plains; mean (Apr–May)	56	47	Morcrette (2002)
U-NSW	34.39°S, 145.30°E	94	Semi-arid; mean (1 yr)	35	25	Wild and Cechet (2002)
Global	—	—	Model calculation	62	46	Kiehl and Trenberth (1997)

Satellite Cloud Climatology Project (ISCCP) datasets that were greater than our estimates. This is potentially due to errors in cloud cover estimates in the two products (Town et al. 2005). Briegleb and Bromwich (1998) used ground-based pyrgeometer data from the South Pole and calculated an annual mean LNCRF of 1 W m^{-2}. To get the clear-sky fluxes without reference to cloud observations they took minimum values of upward and downward flux for the entire month to represent clear-sky conditions.

6. Fractional cloud cover

As stated earlier, FCC at high latitudes based on nighttime visual observations (FCC_{vis}) is relatively uncertain. To accurately report FCC_{vis}, the observers are required to remain outside long enough for their eyes to become dark-adapted, and to learn the night sky in detail and apply their knowledge to potentially scattered or broken cloud cover. When Hahn et al. (1995) screened the visual observations at the South Pole for adequate moonlight, the computed wintertime FCC_{vis} rose ~10% in comparison with FCC computed using all observations. However, the lunar brightness threshold used by Hahn et al. (1995) was developed for latitudes 0°–50°N. Hahn et al. (1995) admit that there may never be adequate moonlight at the South Pole for a visual observer to accurately determine FCC_{vis} due to the prevalence of thin cirrus clouds, as opposed to the more optically thick clouds prevalent in the regions for which their threshold was developed.

The FCC_{vis}, FCC_{pyr}, and FCC_{PAERI} for 2001 are shown in Fig. 11. The algorithms on which FCC_{pyr} and FCC_{PAERI} are based were detailed in section 3b. Relative to the daylight visual observations in January and February, the pyrgeometer underreports cloud cover. As stated earlier, it may be that the algorithm for deriving cloud cover from the pyrgeometer data is not detecting scattered, thin, or cold clouds. FCC_{PAERI} is also lower than the visual observations in summer. However, the differences from visual reports are within their combined uncertainties for spring, summer, and autumn (Table 5). It is in winter that there are significant disagreements between cloud amounts from the

TABLE 11. Comparison of annual mean observations of LNF and LNCRF for the Antarctic Plateau and other locations. The ISCCP LNF is for the time period of Apr 1986–Apr 1987, and the ISCCP LNCRF is for the time period 1985–93. LNCRF is the same as LDCRF in the global case because the upwelling fluxes of that simulation were the same in both the clear and cloudy cases. The other references from Table 10 did not report net or upwelling fluxes.

Station	Lat, lon	Alt (m)	LNF	LNCRF	Time period	Source
South Pole	90°S	2835	−32	9	2000–01	This work
South Pole	90°S	2835	−26	1	1986–88	Briegleb and Bromwich (1998)
South $Pole_{ISCCP}$	90°S	2835	−27	16	Apr 1986–Apr 1987, 1985–93	Hines et al. (2004); Pavolonis and Key (2003)
South $Pole_{APP\text{-}x}$	90°S	2835	−24	30	1982–99	Hines et al. (2004); Pavolonis and Key (2003)
SHEBA	77°N, 165°W	0	−22	38	Oct 1997–Oct 1998	Intrieri et al. (2002)
Global	—	0	−66	46	–	Kiehl and Trenberth (1997)

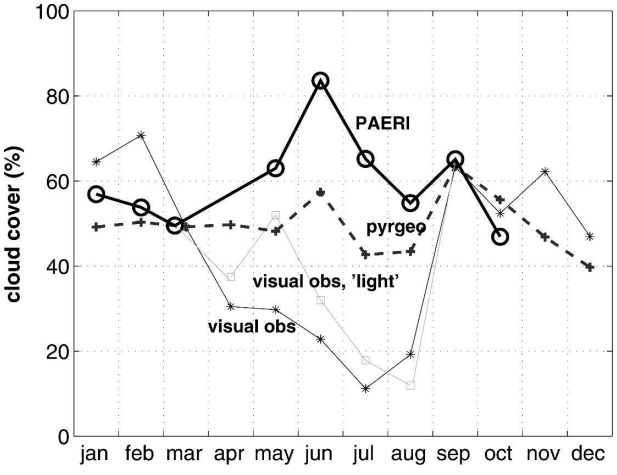

FIG. 11. Monthly mean FCC_{vis}, FCC_{pyr}, and FCC_{PAERI} for 2001. The correction for adequate moonlight for the 2001 visual observations has been included in Fig. 11 for completeness but severely restricts the data available. To qualify as "light," visual observations were used only when the moon was above the horizon and between its first and last quarter. At the South Pole, the nature of the lunar orbit results in two continuous weeks of relative light and two weeks of darkness as the moon rises and sets during the polar night. Applying a moonlight filter to the visual observations on a monthly basis therefore leads to potentially significant sampling errors.

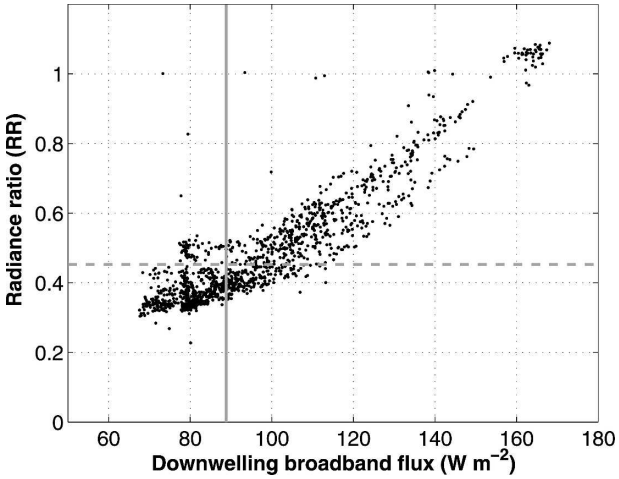

FIG. 12. Scatterplot of Jun radiance ratio (RR) plotted against Jun pyrgeometer measurements. The horizontal dashed line is the CSR threshold for Jun. The vertical solid line is the clear-sky flux threshold for Jun. The number of points is 1384.

irradiance-based estimates of FCC and visual observations.

The FCC_{pyr} shows no seasonal cycle for 2001, while FCC_{PAERI} actually shows greater cloud cover in winter than in summer. However, these two radiation-based estimates of FCC do show similar month-to-month variations. Figure 12 is a scatterplot of radiance ratio from the PAERI plotted against flux from the pyrgeometer for June 2001. It suggests that these two methods are measuring the same thing even though they have drastically different fields of view. The month of June was chosen as an example because it exhibited the greatest disagreement between FCC_{pyr} and FCC_{PAERI} in Fig. 11. Despite this disagreement, the scatterplot shows good correlation, indicating that perhaps we are correct in our conclusion that the FCC_{pyr} algorithm is classifying scattered, thin, or cold clouds as clear sky. This good correlation is a result of the binary character of cloud cover over the South Pole mentioned in section 3b. In addition, the level topography of the Antarctic Plateau prevents scattered clouds from preferentially avoiding the FOV of the PAERI, making FCC_{pyr} and FCC_{PAERI} statistically comparable.

7. Conclusions

Clear-sky downward longwave flux, cloud radiative forcing, and fractional cloud cover were determined for the South Pole based on data collected during the 2001 SPARCLE field season. A strong seasonal cycle is evident in the LDF_{clear} due predominantly to the seasonal cycle of atmospheric temperatures and humidities. Broadband monthly mean LDF_{clear} ranges from 125 W m^{-2} in summer to 70 W m^{-2} in winter. Flux from the water vapor bands accounts for about two-thirds of the broadband LDF_{clear} throughout the year and CO_2 accounts approximately for the other one-third.

The approximately 2:1 ratio across the seasons is due to three factors. Shifting of the frequency of the blackbody emission peak as temperature drops emphasizes the water vapor rotational band over the CO_2 15-μm band. The decrease in atmospheric humidity from summer to winter only slightly reduces the relative water vapor contribution to LDF_{clear} because the water vapor rotational band is mostly saturated. The decrease in atmospheric temperature from summer to winter explains nearly all the decrease in CO_2 flux and the remaining flux due to water vapor. Absorption and reemission of radiation by near-surface diamond-dust crystals during both summer and winter may explain the remaining discrepancies between modeled results and observations.

LDCRF over the East Antarctic Plateau has no apparent seasonal cycle. The mean LDCRF was 23 W m^{-2} in 2001 and 24 W m^{-2} in 1992. These values are about half those typically found at lower-latitude sites. Earlier surface-based observations underestimate LNCRF because of assumptions of LDF and LUF correlations. Satellite-derived estimates of LNCRF are too high probably because of inaccurate cloud cover estimates from the satellite retrievals.

The FCC on which the flux analysis was based was determined from data from an infrared spectrometer (the PAERI). The FCC_{PAERI} agrees with visual observations within the uncertainties of both measurements during times of adequate daylight, but yields higher cloud amounts during the polar night. The visual observations are probably inaccurate during the polar night due to the difficult and subjective nature of the observation.

Acknowledgments. Stephen Hudson helped to collect the SPARCLE dataset, and provided advice and technical assistance. Eric Sandberg and Paulene Roberts, the NOAA 2001 winterover crew, collected the CMDL data. Bryan Johnson, Thomas Mefford, and Ellsworth Dutton provided the data and metadata from the CMDL in a timely manner. Ellsworth Dutton provided information about the maintenance and calibration of the CMDL pyrgeometer. Michael Pavolonis and Jeff Key provided us with APP-x data. Keith Hines provided us with some cloud forcing data, and excellent comments and suggestions. Penny Rowe assisted us in using LBLRTM. Qiang Fu provided insightful comments and suggestions. We appreciate the useful comments of two anonymous reviewers. This work was supported by NSF Grants OPP-9726676 and OPP-0230466.

REFERENCES

Allan, R. P., 2000: Evaluation of simulated clear-sky longwave radiation using ground-based observations. *J. Climate,* **13,** 1951–1964.

Bell, R. J., 1972: *Introductory Fourier Transform Spectroscopy*. Academic Press, 382 pp.

Briegleb, B. P., and D. H. Bromwich, 1998: Polar radiation budgets of the NCAR CCM3. *J. Climate,* **11,** 1246–1268.

Chamberlin, R. A., 2001: South Pole submillimeter sky opacity and correlations with radiosonde observations. *J. Geophys. Res.,* **106,** 20 101–20 113.

Clough, S. A., and M. J. Iacono, 1995: Line-by-line calculations of atmospheric fluxes and cooling rates. 2: Application to carbon dioxide, ozone, methane, nitrous oxide and the halocarbons. *J. Geophys. Res.,* **100,** 16 519–16 535.

——, ——, and J. L. Moncet, 1992: Line-by-line calculations of atmospheric fluxes and cooling rates: Application to water vapor. *J. Geophys. Res.,* **97,** 15 761–15 785.

Curry, J. A., W. B. Rossow, D. Randall, and J. L. Schramm, 1996: Overview of Arctic cloud and radiation characteristics. *J. Climate,* **9,** 1731–1764.

Dalrymple, P. C., 1966: A physical climatology of the Antarctic Plateau. *Studies in Antarctic Meteorology, Antarctic Research Series,* M. J. Rubin, Ed., Vol. 9, Amer. Geophys. Union, 195–231.

Dutton, E. G., 1993: An extended comparison between LOWTRAN7 computed and observed broadband thermal irradiances: Global extreme and intermediate surface conditions. *J. Atmos. Oceanic Technol.,* **10,** 326–336.

Elliott, W. P., and D. J. Gaffen, 1991: On the utility of radiosonde humidity archives for climate studies. *Bull. Amer. Meteor. Soc.,* **72,** 1507–1520.

Hahn, C. J., S. G. Warren, and J. London, 1995: The effect of moonlight on observation of cloud cover at night, and application to cloud climatology. *J. Climate,* **8,** 1429–1446.

Hines, K. M., R. W. Grumbine, D. H. Bromwich, and R. I. Cullather, 1999: Surface energy balance of the NCEP MRF and NCEP–NCAR reanalysis in Antarctic latitudes during FROST. *Wea. Forecasting,* **14,** 851–866.

——, D. H. Bromwich, P. J. Rasch, and M. J. Iacono, 2004: Antarctic clouds and radiation within the NCAR climate models. *J. Climate,* **17,** 1198–1212.

Houghton, J. T., Y. Ding, D. J. Griggs, M. Noguer, P. J. van der Linden, X. Dai, K. Maskell, and C. A. Johnson, Eds., 2001: *Climate Change 2001: The Scientific Basis.* Cambridge University Press, 881 pp.

Hudson, S. R., and R. E. Brandt, 2005: A look at the surface-based temperature inversion over the Antarctic Plateau. *J. Climate,* **18,** 1673–1696.

——, M. S. Town, V. P. Walden, and S. G. Warren, 2004: Temperature, humidity, and pressure response of radiosondes at low temperatures. *J. Atmos. Oceanic Technol.,* **21,** 825–836.

Intrieri, J. M., C. W. Fairall, M. D. Shupe, P. O. G. Persson, E. L Andreas, P. S. Guest, and R. E. Moritz, 2002: An annual cycle of Arctic surface cloud forcing at SHEBA. *J. Geophys. Res.,* **107,** 8039, doi:10.1029/2000JC000439.

Iziomon, M. G., H. Mayer, and A. Matzarakis, 2003: Downward atmospheric longwave irradiance under clear and cloudy skies: Measurement and parameterization. *J. Atmos. Solar-Terr. Phys.,* **65,** 1107–1116.

Kiehl, J. T., and K. E. Trenberth, 1997: Earth's annual global mean energy budget. *Bull. Amer. Meteor. Soc.,* **78,** 197–208.

Knuteson, R. O., and Coauthors, 2004a: Atmospheric Emitted Radiance Interferometer (AERI). Part I: Instrument design. *J. Atmos. Oceanic Technol.,* **21,** 1763–1776.

——, and Coauthors, 2004b: Atmospheric Emitted Radiance Interferometer (AERI). Part II: Instrument performance. *J. Atmos. Oceanic Technol.,* **21,** 1777–1789.

Kuhn, M., A. J. Riordan, and I. A. Wagner, 1975: The climate of Plateau Station. *Climate of the Arctic,* G. Weller and S. A. Bowling, Eds., Geophysical Institute, University of Alaska, 255–267.

——, L. S. Kundla, and L. A. Stroschein, 1977: The radiation budget at Plateau Station, Antarctica, 1966–67. *Meteorological Studies at Plateau Station, Antarctic Research Series,* J. A. Businger, Ed., Vol. 25, Amer. Geophys. Union, 41–73.

Mahesh, A., V. P. Walden, and S. G. Warren, 1997: Radiosonde temperature measurements in strong inversions: Correction for thermal lag based on an experiment at the South Pole. *J. Atmos. Oceanic Technol.,* **14,** 45–53.

——, ——, and ——, 2001a: Ground-based infrared remote sensing of cloud properties over the Antarctic Plateau. Part I: Cloud-base heights. *J. Appl. Meteor.,* **40,** 1265–1278.

——, ——, and ——, 2001b: Ground-based infrared remote sensing of cloud properties over the Antarctic Plateau. Part II: Cloud optical depths and particle sizes. *J. Appl. Meteor.,* **40,** 1279–1294.

Marty, C., and R. Philipona, 2000: The clear-sky index to separate clear-sky from cloudy-sky situations in climate research. *Geophys. Res. Lett.,* **27,** 2649–2652.

——, and Coauthors, 2003: Downward longwave irradiance uncertainty under arctic atmospheres: Measurements and modeling. *J. Geophys. Res.,* **108,** 4358, doi:10.1029/2002JD002937.

Miloshevich, L. M., H. Vömel, A. Paukkunen, A. J. Heymsfield, and S. J. Oltmans, 2001: Characterization and correction of relative humidity measurements from Vaisala RS80-A radiosondes at cold temperatures. *J. Atmos. Oceanic Technol.,* **18,** 135–156.

Morcrette, J.-J., 2002: Assessment of the ECMWF model cloudiness and surface radiation fields at the ARM SGP site. *Mon. Wea. Rev.,* **130,** 257–277.

Pavolonis, M. J., and J. R. Key, 2003: Antarctic cloud radiative forcing at the surface estimated from the AVHRR Polar Pathfinder and ISCCP D1 datasets, 1985–1993. *J. Appl. Meteor.,* **42,** 827–840.

Philipona, R., and Coauthors, 2001: Atmospheric longwave irradiance uncertainty: Pyrgeometers compared to an absolute sky-scanning radiometer, atmospheric emitted radiance interferometer, and radiative transfer model calculations. *J. Geophys. Res.,* **106,** 28 129–28 141.

Ramanathan, V., R. D. Cess, E. F. Harrison, P. Minnis, B. R. Barkstrom, E. Ahmad, and D. Hartmann, 1989: Cloud-radiative forcing and climate: Results from the Earth Radiation Budget Experiment. *Science,* **243,** 57–63.

Rowe, P. M., 2004: Measurements of the Foreign-Broadened Continuum of Water Vapor in the 6.3 micron band at −30° Celsius. Ph.D. thesis, University of Washington, 258 pp.

Schwerdtfeger, W., 1984: *Weather and Climate of the Antarctic.* Elsevier, 261 pp.

Sutter, M., B. Dürr and R. Philipona, 2004: Comparison of two radiation algorithms for surface-based cloud-free sky detection. *J. Geophys. Res.,* **109,** D17202, doi:10.1029/2004JD004582.

Tobin, D. C., and Coauthors, 1999: Downwelling spectral radiance observations at the SHEBA ice station: Water vapor continuum measurements from 17 to 26 μm. *J. Geophys. Res.,* **104,** 2081–2092.

Town, M. S., V. P. Walden, and S. G. Warren, 2005: Cloud cover climatology for the South Pole from surface-based infrared radiation measurements. Preprints, *Eighth Conf. on Polar Meteorology and Oceanography,* San Diego, CA, Amer. Meteor. Soc., CD-ROM, P1.26.

Vaisala, 1997: RS80 manufacturer's brochure. Vaisala, Tech. Rep. A571 1997–8, 2 pp.

Walden, V. P., 1995: The downward longwave radiation spectrum over the Antarctic Plateau. Ph.D. thesis, University of Washington, 267 pp.

——, S. G. Warren, and F. J. Murcray, 1998: Measurements of the downward longwave radiation spectrum over the Antarctic Plateau and comparisons with a line-by-line radiative transfer model for clear skies. *J. Geophys. Res.,* **103,** 3825–3845.

——, and Coauthors, 2001: The South Pole atmospheric radiation and cloud lidar experiment (SPARCLE). Preprints, *Sixth Conf. on Polar Meteorology and Oceanography,* San Diego, CA, Amer. Meteor. Soc., 297–299.

——, S. G. Warren, and E. Tuttle, 2003: Atmospheric ice crystals over the Antarctic Plateau in winter. *J. Climate,* **42,** 1391–1405.

Warren, S. G., 1996: Antarctica. *Encyclopedia of Climate and Weather,* S. H. Schneider, Ed., Oxford University Press, 31–39.

——, C. J. Hahn, J. London, R. M. Chervin, and R. L. Jenne, 1986: Global distribution of total cloud cover and cloud type amounts over land. NCAR, TN-273+STR, 29 pp. + 200 maps.

Wild, M., and R. Cechet, 2002: Downward longwave radiation in general circulation models: A case study at a semi-arid continental site. *Tellus,* **54A,** 330–337.